

SI Appendix

Section I. Energy dependence of the Fourier transforms of dI/dV maps

CDW- $2a_0$ region

To demonstrate that the CDW- $2a_0$ wave vector (\mathbf{Q}_{2a_0}) maintains the same magnitude as a function of STM bias, we examine a series of FTs of dI/dV maps acquired in a range of STM biases (Figure S1(d)) and their associated FT linecuts (Figure S1(e)). As can be seen, $|\mathbf{Q}_{2a_0}|$ is located exactly at $0.5|\mathbf{Q}_{\text{Bragg}}|$, thus confirming its commensurate nature. Moreover, the position of this peak does not

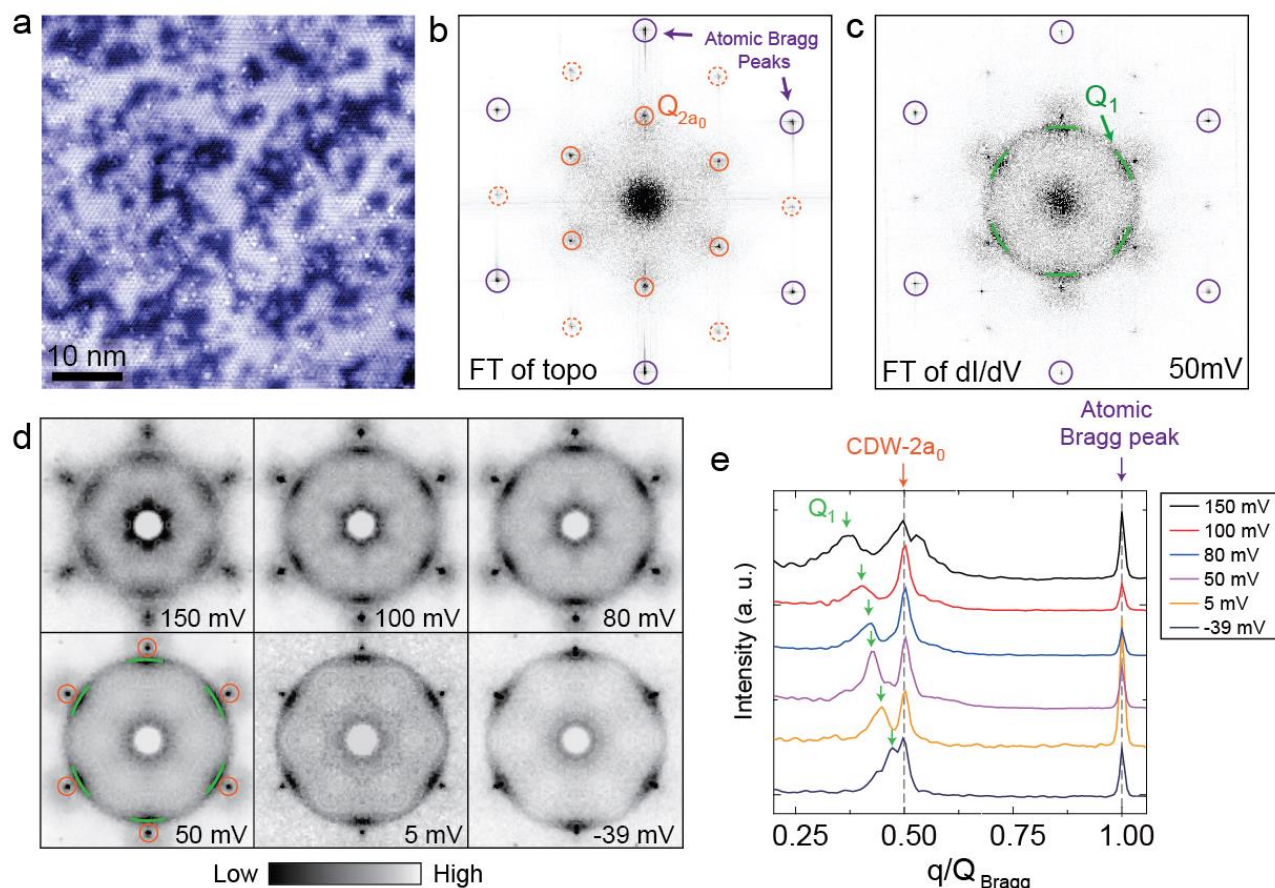


Figure S1. CDW- $2a_0$ wave vectors as a function of energy. (a) STM topograph and (b) associated FT of the region of the sample where the data was taken. (c) FT of a dI/dV map at 50 mV. Prominent peaks are denoted as: \mathbf{Q}_{2a_0} (solid orange circles), satellite peaks of \mathbf{Q}_{2a_0} (dashed orange circles), \mathbf{Q}_1 (green lines) and atomic Bragg peaks (purple circles). (d) A series of 6-fold symmetrized FTs of dI/dV maps at different bias, each zoomed-in closer to the center of the FT compared to (c) to emphasize the prominent features. Bragg peaks in (d) are outside of each square region plotted and therefore not visible. (e) A series of linecuts acquired along the Γ - M direction from the FTs in (d). Center of the FTs in (d) has been artificially suppressed to emphasize other features. Setup in (a): $I_{\text{set}} = 350$ pA, $V_{\text{sample}} = -60$ mV.

disperse with energy (Figure S1(e)), therefore ruling out dispersive QPI signal as the cause of our observations. In contrast, the Q_1 peak exhibits a clear dispersion.

CDW- $4a_0$ region

Similarly, to visualize the evolution of various peaks in the FT as a function of STM bias, we focus on a large region of the sample (to increase q -space resolution), which hosts smaller domains of CDW- $4a_0$ oriented primarily along two different lattice directions (Figure S2(a,b)). First, to demonstrate the non-dispersive nature of the CDW- $4a_0$ wave vector (Q_{4a_0}), we examine a series of FTs of dI/dV

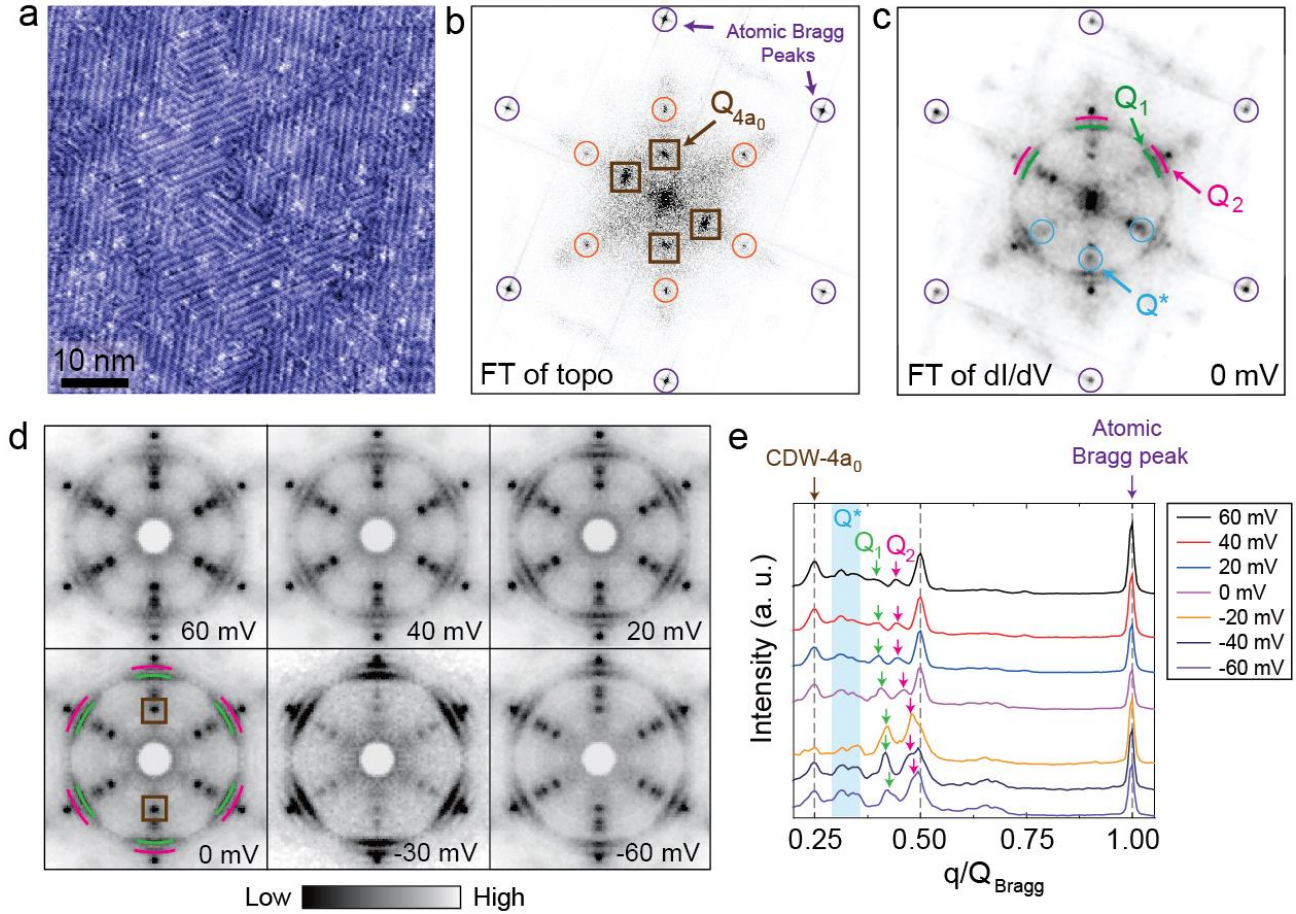


Figure S2. CDW- $4a_0$ wave vectors as a function of energy. (a) STM topograph and (b) associated FT of the region of the sample where the data was taken. (c) FT of a dI/dV map at 0 mV with prominent peaks denoted: Q_{4a_0} (brown squares), Q_1 (green line), Q_2 (pink line), atomic Bragg peaks (purple circles) and $Q_{\text{Bragg}}/2$ (orange circles). (d) A series of 6-fold symmetrized FTs of dI/dV maps at different bias, each zoomed-in closer to the center of the FT compared to (c) to emphasize the prominent features. Bragg peaks in (d) are outside of each square region plotted and therefore not visible. (e) A series of linecuts acquired along the Γ -M direction from the FTs in (d). CDW- $4a_0$ is intrinsically a unidirectional order, so the six-fold symmetry of the Q_{4a_0} peaks in (d) is an artifact of the symmetrization process. The center of the FTs in (d) has been artificially suppressed to emphasize other features. The FT in (c) was smoothed with a local averaging circle of $\sim 0.02 \text{ \AA}^{-1}$ radius. Setup in: (a) $I_{\text{set}} = 200 \text{ pA}$, $V_{\text{sample}} = 140 \text{ mV}$; (d) $I_{\text{set}} = 320 \text{ pA}$, $V_{\text{sample}} = -60 \text{ mV}$ and $V_{\text{exc}} = 10 \text{ mV}$ (zero-to-peak).

maps acquired in a range of STM biases (Figure S2(d)) and their associated FT linecuts (Figure S2(e)). As can be seen, $|\mathbf{Q}_{4a_0}|$ is located exactly at $0.25|\mathbf{Q}_{\text{Bragg}}|$, thus confirming its commensurate nature. Moreover, the position of this peak does not disperse with energy, thus ruling out dispersive QPI signal as the cause of our observations. We note that although our field of view contains CDW- $4a_0$ domains oriented along 2 different lattice directions, the observed CDW- $4a_0$ order is clearly unidirectional in any given region of the sample. In contrast to the non-dispersive peaks observed, \mathbf{Q}_1 and \mathbf{Q}_2 peaks exhibit a clear dispersion, decreasing in magnitude with increased energy (Figure S2(e)).

The FT of the STM topograph, related to the integral of the density of states from the Fermi level to the setup bias, clearly shows the dominant \mathbf{Q}_{4a_0} vectors and the atomic Bragg peaks (Figure S2(b)). However, we also observe additional faint peaks in the FTs. First, a broad peak (\mathbf{Q}^*), possibly faintly observed in the topograph FT but more clearly seen in the FT of dI/dV maps, appears along all Γ -M directions and is non-dispersive with energy (Figure S2(c)). Its position (determined by fitting a single 2D Gaussian in the FTs in Figure S2(d)) is $\sim 0.33|\mathbf{Q}_{\text{Bragg}}|$, nearly identical to that of conventional CDW- $3a_0$ seen in NbSe₂. We also observe additional weak peaks at exactly $0.5|\mathbf{Q}_{\text{Bragg}}|$ along all Γ -M directions (orange circles in Figure S2(b)). These can be partially explained by the satellite reflections of the \mathbf{Q}_{4a_0} peaks. However, this cannot be the entire explanation as these peaks appear along all 3 lattice directions even if only a single \mathbf{Q}_{4a_0} peak is present (Fig. 1(f) of the main text). We hypothesize that \mathbf{Q}^* and $0.5|\mathbf{Q}_{\text{Bragg}}|$ peaks could possibly be related to the remnant of the other CDW phases still existing in patches, possibly pinned by defects, in the otherwise dominant CDW- $4a_0$ region. This may be another indication of how incredibly close to a degenerate (critical) point this system is. However, further work is needed to fully understand this picture.

Section II. Drift field extraction and strain analysis of STM topographs

We describe in detail how the Lawler-Fujita algorithm¹ can be used to extract local variations in lattice strain from STM topographs. The section is split into two parts: (1) extraction of the total displacement field $\mathbf{u}(\mathbf{r})$, and (2) disentangling the real strain field $\mathbf{s}(\mathbf{r})$ from the experimental artifacts inevitably present in $\mathbf{u}(\mathbf{r})$.

The extraction of total displacement field $\mathbf{u}(\mathbf{r})$

Atomically-resolved STM topographs typically contain some atomic spatial deviation from the ideal atomic arrangement, which we refer to as the total displacement field $\mathbf{u}(\mathbf{r})$. This field can be extracted using the well-established Lawler-Fujita algorithm¹, which we have previously applied on a range of different materials²⁻⁴. In the following sub-section, we briefly describe the method.

The surface of NbSe₂ is composed of Selenium atoms, which have a hexagonal lattice with lattice constant $a \sim 0.31$ nm. An STM topograph $T(\mathbf{r})$ of a hexagonal lattice can be represented by:

$$T(\mathbf{r}) \approx A_1 e^{i\mathbf{Q}_1 \cdot (\mathbf{r} - \mathbf{u}_1(\mathbf{r}))} + A_2 e^{i\mathbf{Q}_2 \cdot (\mathbf{r} - \mathbf{u}_2(\mathbf{r}))} + A_3 e^{i\mathbf{Q}_3 \cdot (\mathbf{r} - \mathbf{u}_3(\mathbf{r}))} + \text{c. c.} \quad (1)$$

where \mathbf{Q}_1 and \mathbf{Q}_2 are the reciprocal lattice basis, each with magnitude of $4\pi/(\sqrt{3}a)$, and oriented 120° with respect to one another. In the third term in Equation (1), \mathbf{Q}_3 has the same magnitude as previous two and points to the third direction, i.e. $\mathbf{Q}_3 = \mathbf{Q}_2 + \mathbf{Q}_1$. $u_i(\mathbf{r})$ called the displacement component in the i^{th} direction, is the projection of $\mathbf{u}(\mathbf{r})$ onto \mathbf{Q}_i direction:

$$u_i(\mathbf{r}) = \mathbf{u}(\mathbf{r}) \cdot \hat{\mathbf{Q}}_i \quad (i = 1, 2, 3) \quad (2)$$

Given any two of these three scalar fields, we can calculate the total displacement field $\mathbf{u}(\mathbf{r})$.

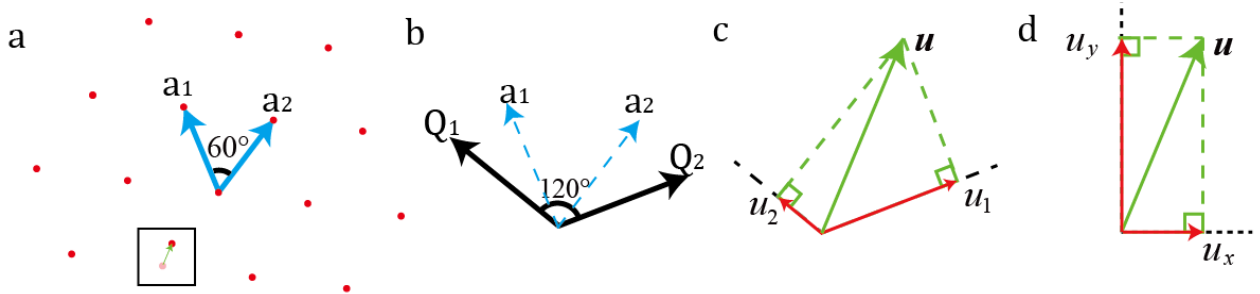


Figure S3. The real space and the reciprocal space vectors. (a) The schematic of the hexagonal real-space Se lattice in the top layer and the two basis vectors \mathbf{a}_1 and \mathbf{a}_2 . The square shows an example of a displacement field vector $\mathbf{u}(\mathbf{r})$ at a certain lattice position, where the atom is displaced by the vector indicated by the green arrow. (b) Reciprocal lattice vectors derived from \mathbf{a}_1 and \mathbf{a}_2 . (c) Sketch of the total displacement field $\mathbf{u}(\mathbf{r})$ and its components $u_1(\mathbf{r})$ and $u_2(\mathbf{r})$ along \mathbf{Q}_1 and \mathbf{Q}_2 respectively, at the lattice point in (a). Displacement field components $u_1(\mathbf{r})$ and $u_2(\mathbf{r})$ can be derived from $\mathbf{u}(\mathbf{r})$ by projecting $\mathbf{u}(\mathbf{r})$ onto \mathbf{Q}_1 and \mathbf{Q}_2 directions. (d) $\mathbf{u}(\mathbf{r})$ decomposed into u_x and u_y components along \mathbf{x} and \mathbf{y} scanning frame directions for convenience.

By applying the procedure thoroughly explained in Ref. ¹, we can get the two displacement field components $u_1(\mathbf{r})$ and $u_2(\mathbf{r})$. For computational simplicity, it is desirable to decompose these into two new components along x and y axes: $u_x(\mathbf{r})$ and $u_y(\mathbf{r})$ (Figure S3(d)). The input to the Lawler-Fujita algorithm are the atomic Bragg peak positions in the Fourier transform of the topograph obtained by 2D Gaussian fitting, and a spatial smoothing length scale L ($L = 1/\Lambda_u$ as defined in Ref. ¹). L used

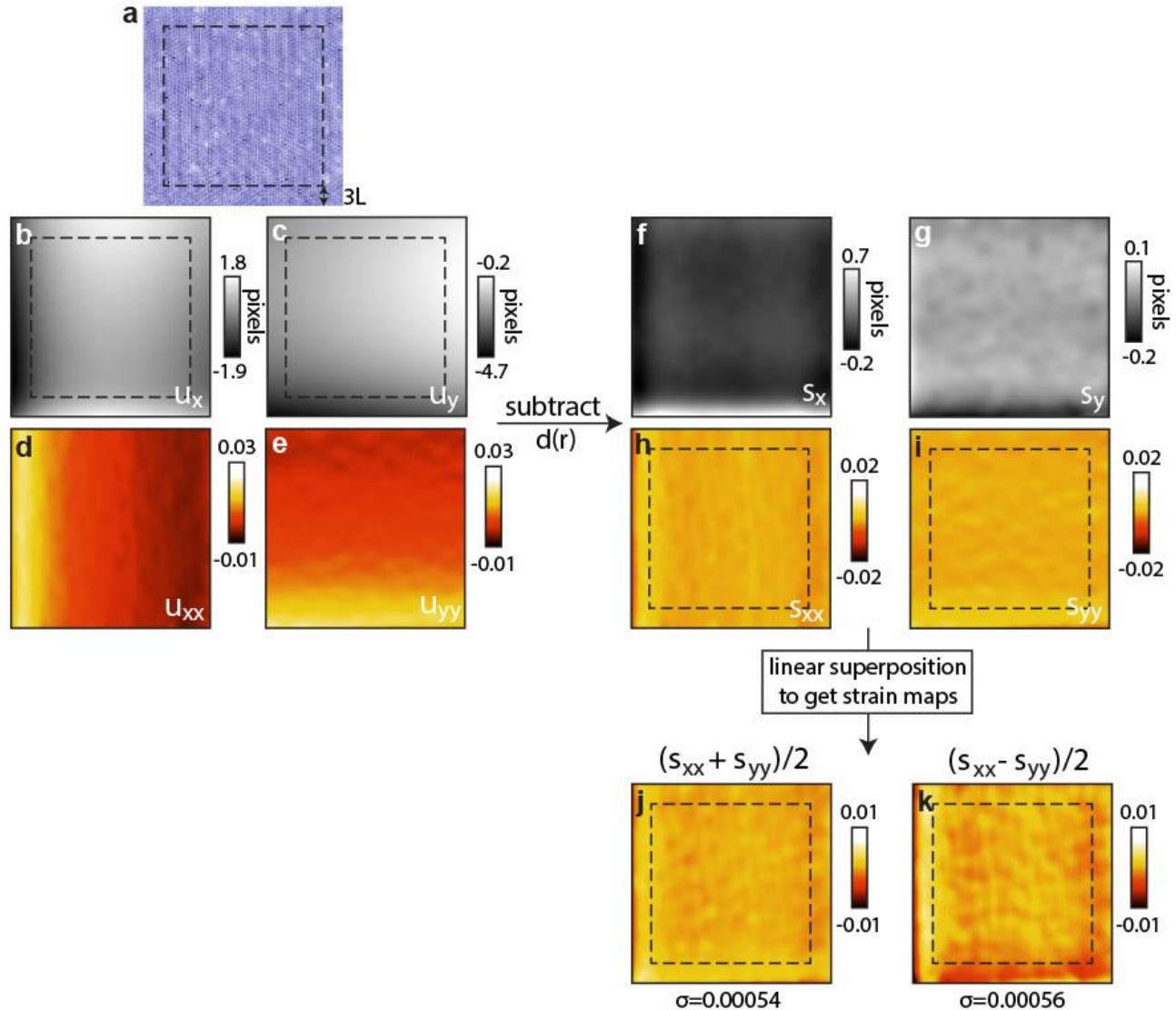


Figure S4. Application of the strain algorithm to an STM topograph hosting exclusively CDW-3a₀. (a) STM topograph of a 50 nm square region (688 x 688 pixels) acquired at -100 mV/40 pA and 100 nm/sec tip speed. The scan started at the lower left corner, scanning upwards after it was in feedback over the same area of the sample for ~30 minutes. (b-e) u_x , u_y , u_{xx} and u_{yy} fields obtained from the topograph in (a) using the Lawler-Fujita algorithm. (f,g) Strain field components s_x and s_y obtained from (b,c) by subtracting a 3rd degree polynomial fit to the central square region (square dashed line in (a)). (h,i) Gradients of the strain field s_{xx} and s_{yy} . (j) Biaxial strain map and (k) uniaxial strain map obtained by linear superposition of the (h,i). Standard deviations of all the values inside square regions in (j,k) are denoted below the images. Dashed square outline in (h,i,j,k) are placed at the identical position as the equivalent square in (a).

in this work was $5a$ (a is the lattice constant), and it is converted to the units of pixels. The smoothing kernel used is a Gaussian function $\frac{1}{2\pi L^2} e^{-\frac{r^2}{2L^2}}$ defined on a square with $6L + 1$ side length (in the unit of pixels).

Disentangling intrinsic strain field $s(r)$ from thermal/piezo drift field $d(r)$

There are two main types of contributions to the displacement fields $u_x(\mathbf{r})$ and $u_y(\mathbf{r})$: (1) the actual structural strain, which we will refer to as the strain field with $s_x(\mathbf{r})$ and $s_y(\mathbf{r})$ components, and (2) experimental artifacts, such as piezo-related effects (piezo relaxation/hysteresis, non-linearity) and thermal effects, which we will refer to as the drift field with $d_x(\mathbf{r})$ and $d_y(\mathbf{r})$ components. So, we can write: $u_x(\mathbf{r}) = s_x(\mathbf{r}) + d_x(\mathbf{r})$ and $u_y(\mathbf{r}) = s_y(\mathbf{r}) + d_y(\mathbf{r})$. For the remainder of the section, for simplicity, we will omit writing the “ r ” dependence in the strain field and drift field components.

Fields d_x and d_y are inevitably non-zero, varying spatially across the field-of-view. In our experiments, STM temperature is stable within ~ 1 mK over the course of data acquisition of a single topograph (at the order of 1 hour), so the main contribution to the drift fields comes from piezo-related effects. These effects result in artificial stretching of the topograph, both in the up-down and left-right directions, most pronounced at the start of the scan and on the side-edge where the scan started. We will demonstrate that these piezo effects are sufficiently well-described by a 3rd degree polynomial fit to u_x and u_y . After obtaining d_x and d_y by this fit, it immediately follows that $s_x = u_x - d_x$ and $s_y = u_y - d_y$.

We start with a raw STM topograph of a typical region of a NbSe₂ sample hosting CDW-3a₀, and extract the displacement fields and their derivatives (Figure S4(b-e)). We define partial derivatives as $u_{xx} = \partial_x u_x$ and $u_{yy} = \partial_y u_y$. First, we notice that u_x and u_y vary smoothly across the field-of-view (FOV) and that u_{xx} (u_{yy}) exhibits a gradual evolution from left-to-right (bottom-to-top). These are consistent with the artifacts related to piezo relaxation for scan that started in the lower-left corner of the image (we checked the “backwards” scan starting in the lower-right corner, and the contrast in Figure S4(d) is reversed). We then fit a 3rd degree polynomial plane to the region of u_x (or u_y) denoted by the dashed square to obtain d_x (or d_y), and calculate $s_x = u_x - d_x$ and $s_y = u_y - d_y$ (Figure S4(f,g)). We note that we fit the smaller dashed square as opposed to the whole FOV because: (1) piezo relaxation is typically more pronounced at the edges which might involve higher level polynomial terms, and (2) additional artifacts near the edges associated with the Lawler-Fujita kernel of size $6L+1$ when it is partially placed outside of the FOV (the kernel is partially outside when its center is $3L$ pixels away from all the edges).

Partial derivatives $s_{xx} = \partial_x s_x$, $s_{xy} = \partial_x s_y$, $s_{yx} = \partial_y s_x$ and $s_{yy} = \partial_y s_y$ (s_{xx} and s_{yy} shown in Figure S4(h,i)) are the components of the strain tensor from elasticity theory⁵. It is important to note that the resulting partial derivatives of \mathbf{s} (Figure S4(h,i)) do not show the gradual evolution in left-to-right and up-to-down directions seen in \mathbf{u} (Figure S4(d,e)), which demonstrates that we have sufficiently removed the piezo relaxation effects. The linear combination of the strain tensor components $(s_{xx} + s_{yy})/2$ represents the biaxial strain map (Figure S4(j)), while $(s_{xx} - s_{yy})/2$ is an approximate measure of the uniaxial strain (Figure S4(k)). The average in both maps within the dashed square is nearly zero

($\sim 10^{-6}$) and standard deviation σ is $\sim 5 \cdot 10^{-4}$. The latter value (0.05% change in the lattice constant a) provides an approximate bound on the error of the algorithm. Importantly, we can see that the variations in measured strain presented in Fig. 2 of the main text are **>20 times larger** than σ obtained in Figure S4, and thus significantly higher than our error.

We note that any smoothly varying strain at the order of the 3rd degree polynomial is assumed to be an artifact of the piezo-relaxation, and will not be detected using this algorithm. For example, if there is a uniform strain across the entire FOV (i.e. the whole lattice is stretched uniformly along one direction), this will also be contained in d_x and d_y , and will not be detected in the strain field. However, this algorithm can still be used to reliably detect spatially varying strain with respect to a reference region, as performed in Figure 2 and explained in detail in the following paragraphs.

We turn to the analysis of a topograph hosting different CDW phases (Figure S5(a)), with the goal of comparing the **relative strain** between different CDW regions. The STM topograph is acquired

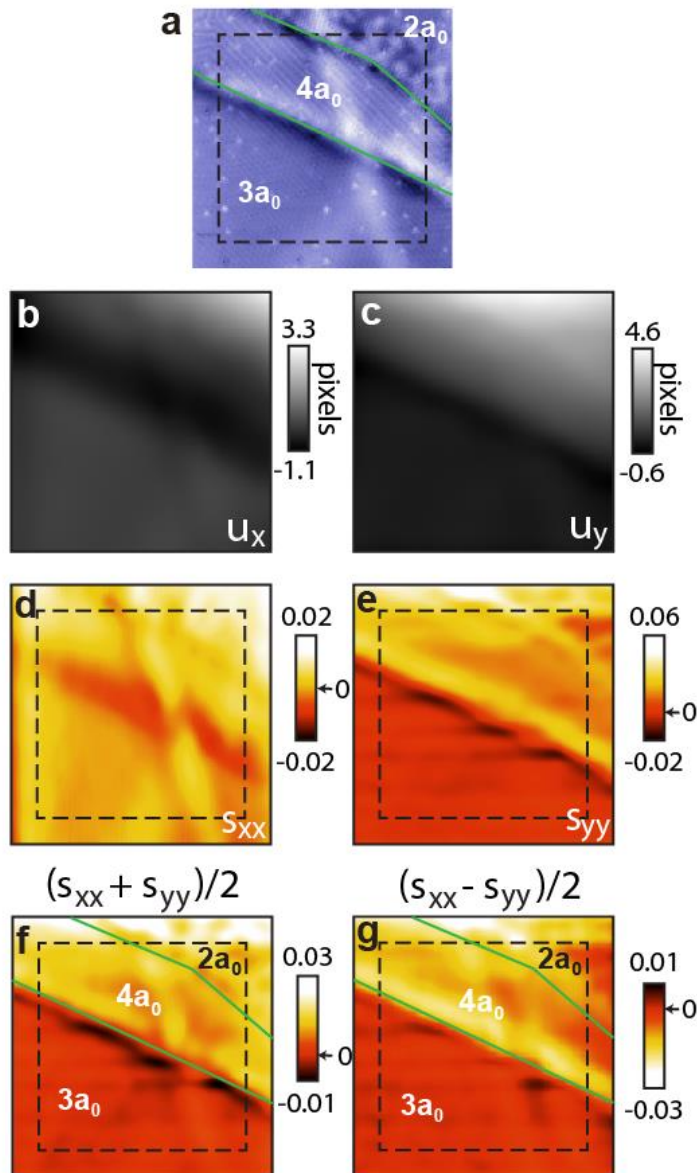


Figure S5. Determination of strain fields in a region with multiple types of CDWs.

(a) STM topograph of a 46 nm square region (448 x 448 pixels) acquired at -100 mV/100 pA and 25 nm/sec tip speed. The scan started in the upper left corner, scanning downwards after it was in feedback over the same area of the sample for ~ 20 minutes. Green lines are an approximate outline of regions hosting different CDW phases. (b,c) u_x and u_y obtained from the topograph in (a) using the Lawler-Fujita algorithm. (d,e) Derivative of strain field components: s_{xx} and s_{yy} . Strain field components s_x and s_y were obtained from (b,c) by subtracting a 3rd degree polynomial fit to the CDW-3a0 region in the bottom left part of the topograph. (f) Biaxial strain map and (g) uniaxial strain map obtained by linear superposition of (d,e). Dashed square outlines in (d,e,f,g) are placed at the identical position as the equivalent square in (a), which is $3L$ distance from the edge of the FOV on all sides.

under comparable conditions as the test topograph in Figure S4 (similar relaxation time, slightly lower scan speed). First, we notice that the displacement field components u_x and u_y obtained from this topograph already show sudden changes exactly at the boundary between different CDWs, which is the first sign of structural strain. To get d_x and d_y , we fit the 3rd degree polynomial, but to the CDW- $3a_0$ region only (lower-left part of the image below the lower green line in Figure S5(a), again excluding the area within $3L$ from the edges), and extrapolate the same fit to obtain d_x and d_y across the entire FOV. By doing this, we make an implicit assumption that the average strain in the CDW- $3a_0$ region is zero. This is a reasonable assumption, given that previous work reported that in-plane strain as small as $\sim 0.06\%$ can already lead to a CDW transition⁶. The rest of the extraction procedure is equivalent to that in Figure S4, and we can obtain the strain maps (Figure S5(f,g)). In the CDW- $4a_0$ region directly adjacent to the CDW- $3a_0$ region, we can clearly see a relative tensile strain of both uniaxial and biaxial type. We note that Fig. 2(b) of the main text is cropped from the boundary in the topograph in Figure S5.

Discussion of the induced strain

First, we discuss the discrepancy between the nominal strain applied to the bottom of the sample ($\sim 0.15\%$) due to the thermal expansion coefficient (TEC) mismatch with the substrate, and the relative local strain observed from STM topographs with spatially varying magnitude at the order of $\sim 1-2\%$. There are several plausible scenarios that could account for this difference. First, we hypothesize that warping of the surface of NbSe₂ could lead to the larger strain observed at the surface. This could plausibly occur due to the way the sample is glued to the substrate, with inhomogeneous distribution of glue at the interface, partially running up the sides of the sample. The resulting behavior observed on the surface may not be very surprising given the van der Waals nature of NbSe₂ and occasionally observed “ripples” in the same material⁶. Another contributing factor might entail an additional, small change in the lattice constant associated with each new CDW phase, although this is likely to be much less than 1%. We also note that the boundary region

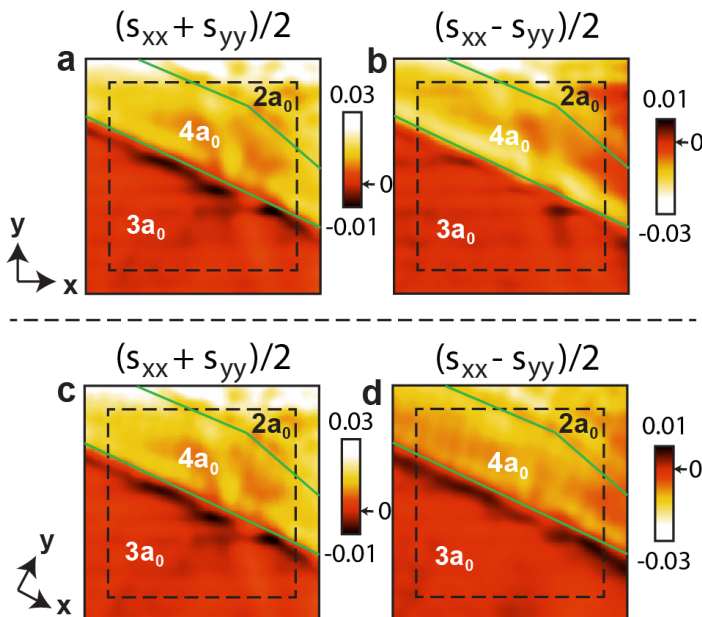


Figure S6. Comparison of strain maps for different coordinate system axis. (a) Biaxial strain map and (b) uniaxial strain map from Figure S5(f,g). (c) Biaxial strain map and (d) uniaxial strain map for the same STM topograph and the coordinate system rotated by ~ 30 degrees clockwise so that the y-axis is perpendicular to the boundary between CDW- $3a_0$ and CDW- $4a_0$. The biaxial maps in (a,c) are identical, while the uniaxial maps display some differences in magnitude.

between the CDW- $3a_0$ and the new CDW phases hosts narrow regions of compressive strain relative to the CDW- $3a_0$ area (dark red/black regions in Fig. 2(c,d) and Figure S6), which would reduce the average strain within the field-of-view, bringing it closer to the expected value from the TEC mismatch. It is also possible that the CDW- $3a_0$ region is under small compressive strain. In this last scenario, the average strain measured over the entire field-of-view would again be reduced, and therefore closer to the average expected value. Finally, the measured strain of $\sim 2\%$ near the boundary is likely to “relax” away from it, in analogy to the strain observed in graphene nano-bubbles that is much more pronounced at the edge (Fig. 3 in Lu et al., *Nature Commun.* 3, 823 (2012)) The combination of all these effects is likely responsible for the relatively large relative strain observed at the surface.

2H-NbSe₂ studied here is the most stable form of bulk NbSe₂, but NbSe₂ can in principle exist in several other much less common forms ⁷. Out of these, the two phases that are stable at low temperature (one of which is the 2H-phase) have nearly identical in-plane lattice constants. The other two phases have $\sim 1\text{-}2\%$ larger lattice constants compared to the 2H-phase, but are only stable at significantly higher temperatures > 1000 C. Aside from the monolayer and the bulk 2H-NbSe₂ which show metallic behavior and 3×3 CDW, the only other phase that has been studied in some detail is the monolayer of 1T-NbSe₂. However, this phase shows a vastly different band structure than 2H-NbSe₂, with a large insulating gap of ~ 0.4 eV and $\sqrt{13} \times \sqrt{13}$ CDW ⁸, neither of which we observed in our experiments. Given the similarity between our QPI measurements in CDW- $2a_0$ /CDW- $4a_0$ regions and those measured on CDW- $3a_0$ 2H-NbSe₂ ⁹, the most likely scenario is that regions hosting the new CDWs are still in the 2H-phase.

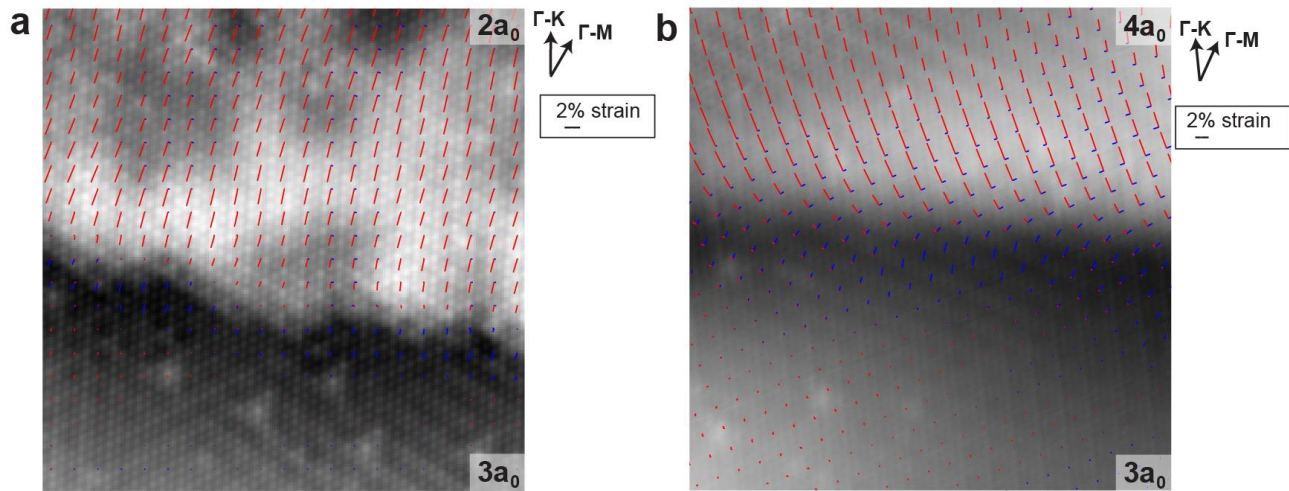


Figure S7. Maps of the eigenvectors of the strain tensor across the (a) CDW- $3a_0$ /CDW- $2a_0$ and (b) CDW- $3a_0$ /CDW- $4a_0$ domain boundary. STM topographs in the background (each 20 nm square) are cropped from the same topographs also used in Fig. 2. Each data point plotted consists of two perpendicular lines indicating the strain eigenvectors, with the length of the line corresponding to each eigenvalue. Blue color indicates negative (compressive) strain, while the red color denotes positive (tensile) strain.

From the data presented in Figure 2 and Figure S5, we extract the average biaxial strain $(s_{xx} + s_{yy})/2$ in the CDW-4a₀ (CDW-2a₀) region to be ~1.0% (~1.1%) larger compared to the CDW-3a₀ area. Thus we can conclude that biaxial *tensile* strain is present in these regions. Mathematically, $(s_{xx} + s_{yy})/2$ value is robust, and remains the same regardless of the choice of the x and y axis, as long as the two axis are orthogonal to one another. Empirically, this can be seen by rotating the coordinate system by for example ~30 degrees clockwise so that the x axis is aligned parallel the CDW boundary, and calculating the biaxial strain maps. The maps are nearly identical before and after the rotation (Figure S6(a,c)).

Interpreting the uniaxial strain magnitude and direction from the $(s_{xx} - s_{yy})/2$ map is more complex, as $(s_{xx} - s_{yy})/2$ map will depend on the choice of the x and y axis (Figure S6(b,d)). But even after rotating the coordinate system to align with the boundary between CDW-3a₀ and CDW-4a₀, significant amount of uniaxial strain (lattice stretched approximately perpendicular to the boundary) is clearly observed in the CDW-4a₀ region compared to the CDW-3a₀ region we use as a reference.

To spatially illustrate the direction of strain, we perform the following. From the strain matrix S :

$$\begin{bmatrix} s_{xx} & (s_{xy} + s_{yx})/2 \\ (s_{xy} + s_{yx})/2 & s_{yy} \end{bmatrix}$$

and the characteristic equation $\det(S - \lambda I) = 0$, we can calculate the two strain eigenvalues:

$$\lambda_{1,2} = \frac{s_{xx} + s_{yy} \pm \sqrt{(s_{xx} - s_{yy})^2 + (s_{xy} + s_{yx})^2}}{2}$$

and two strain eigenvectors $\vec{v}_{1,2}$ respectively by substituting $\lambda_{1,2}$ into S so that $(S - \lambda_i I) \cdot \vec{v}_i = 0$:

$$\begin{aligned} \vec{v}_1 &= (s_{xy} + s_{yx}, -s_{xx} + s_{yy} + \sqrt{(s_{xx} - s_{yy})^2 + (s_{xy} + s_{yx})^2}) \\ \vec{v}_2 &= (s_{xy} + s_{yx}, -s_{xx} + s_{yy} - \sqrt{(s_{xx} - s_{yy})^2 + (s_{xy} + s_{yx})^2}) \end{aligned}$$

In Figure S7, we plot the maps of the two eigenvectors across the CDW domain boundaries shown in Fig. 2. Stretching of the lattice, much more prominent along one direction, is clearly present in both CDW-4a₀ and CDW-2a₀ regions of the sample.

Section III. Analysis of QPI vectors observed

Our QPI measurements reveal two main scattering vectors Q_1 and Q_2 (Figure S8(a)), which we attribute to the scattering within the inner and outer pocket around Γ for the following reasons. First, their magnitudes are comparable (but slightly different) to what is expected based on ARPES experiments of unstrained NbSe₂¹⁰. Next, we systematically eliminate other possibilities denoted in Figure S8. The inner Γ pocket represents the bonding, while the outer one represents the antibonding combination of the two Nb $d_{3z^2-\gamma^2}$ orbitals (i.e. Ref.¹¹). As such, the inter-pocket scattering around Γ (Q_3) is significantly less likely to occur compared to Q_1 and Q_2 due to different symmetries of the orbital wave-function of the two bands/pockets between which the scattering would occur. Scattering within the Fermi surfaces around each K point ($Q_4 - Q_6$) is also less likely to be observed by STM due to the orbital texture of the bands, which lie entirely in-plane at the K-point¹². Finally, the energy dispersion of Q_7 is opposite to what we observe experimentally (Figure S8) – Q_7 is expected to increase as the energy is increased based on the band structure details, but the QPI vectors observed decrease in magnitude with increased energy (Fig. 3 of the main text).

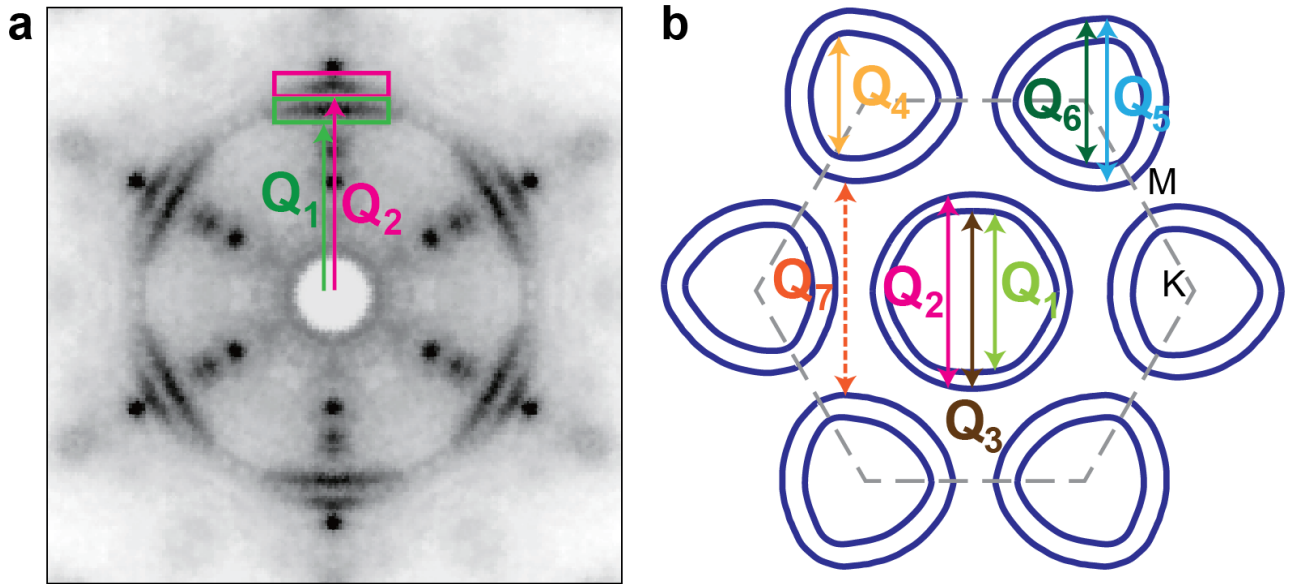


Figure S8. Schematic of the Fermi surface and scattering processes. (a) FT of the dI/dV map obtained at 0 mV over the region of the sample hosting CDW-4a₀, which shows only two peaks along $\Gamma - M$ that disperse with energy, labeled Q_1 and Q_2 . (b) The schematic of the Fermi surface of NbSe₂ with the main possible scattering vectors along $\Gamma - M$ denoted by labels Q_1 to Q_7 . Dashed (solid) lines with arrows in (b) denote if a given vector is expected to increase (decrease) with increased energy.

Section IV. Comparison of QPI dispersions acquired over different CDW regions

Despite the dramatic difference in the CDW wave vector, the band structure extracted from our QPI measurements in CDW-4 a_0 regions is comparable to that obtained by Arguello et al.⁹ on NbSe₂ hosting only a CDW-3 a_0 phase (Figure S9). In contrast to the latter work, however, higher momentum resolution of our data allows us to unambiguously disentangle multiple QPI vectors.

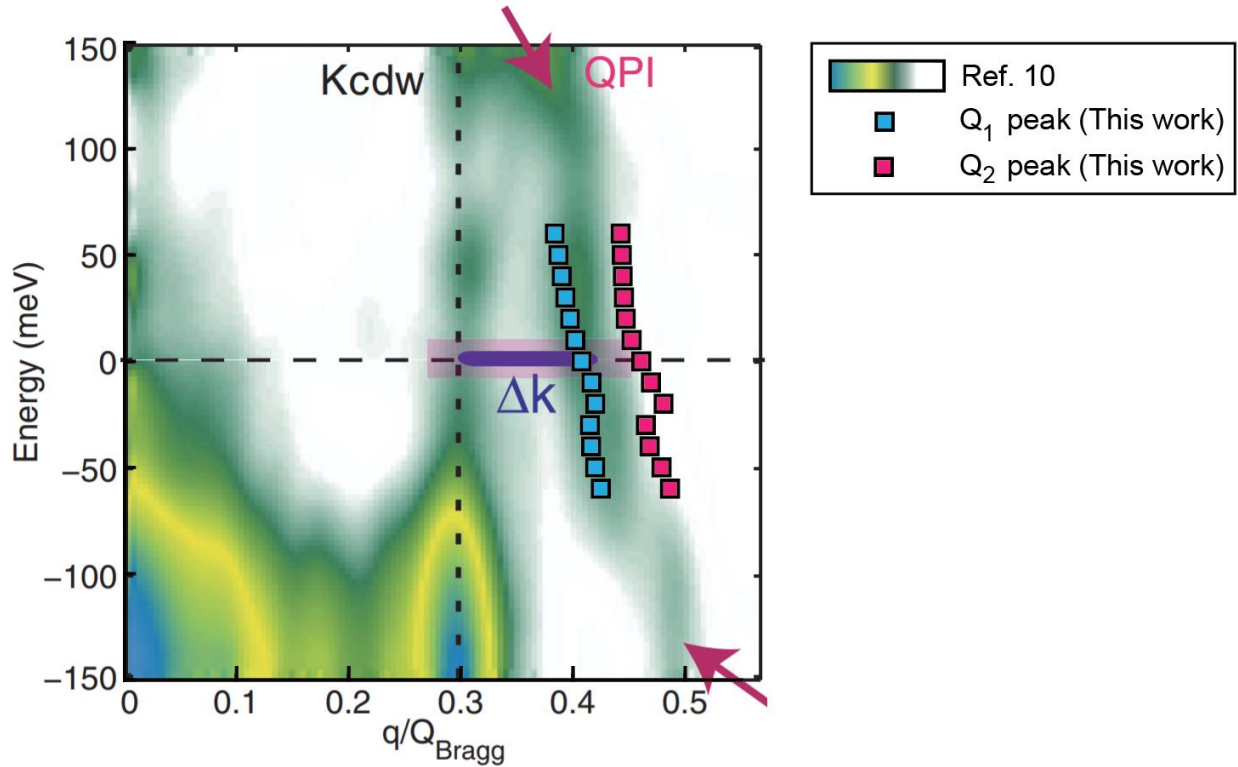


Figure S9. Comparison between QPI dispersions in different CDW regions. Our QPI dispersion data points (blue and pink squares, only) along the Γ -M direction acquired over the CDW-4 a_0 region of the sample (also shown in Fig. 3 of the main text). Our data is then superimposed on top of the QPI data acquired on the Cu-intercalated 2H-NbSe₂ sample that shows a conventional CDW-3 a_0 pattern in Ref.⁹. As it can be seen, the two QPI peaks from the CDW-4 a_0 area have similar wavelengths to the broad QPI peak detected in the CDW-3 a_0 region in Ref.⁹.

Section V. QPI imaging at negative energies

While the QPI wave vectors can be seen at a bias higher than -50 mV in both CDW- $2a_0$ and CDW- $4a_0$ regions of the sample (Figure S10(a-c, e-g)), they disappear at negative energies when the vector magnitude increases to be comparable/larger than $0.5|\mathbf{Q}_{\text{Bragg}}|$ (Figure S10(d,h)). A possible explanation for the lack of signal at higher momenta may be canting of the orbital texture towards more in-plane orientations¹², making them less likely to be detected by the STM tip. This is also consistent with the lack of detection of the \mathbf{Q}_2 peak in the CDW- $2a_0$ area, as its magnitude is likely larger than $0.5|\mathbf{Q}_{\text{Bragg}}|$ in the measured energy range.

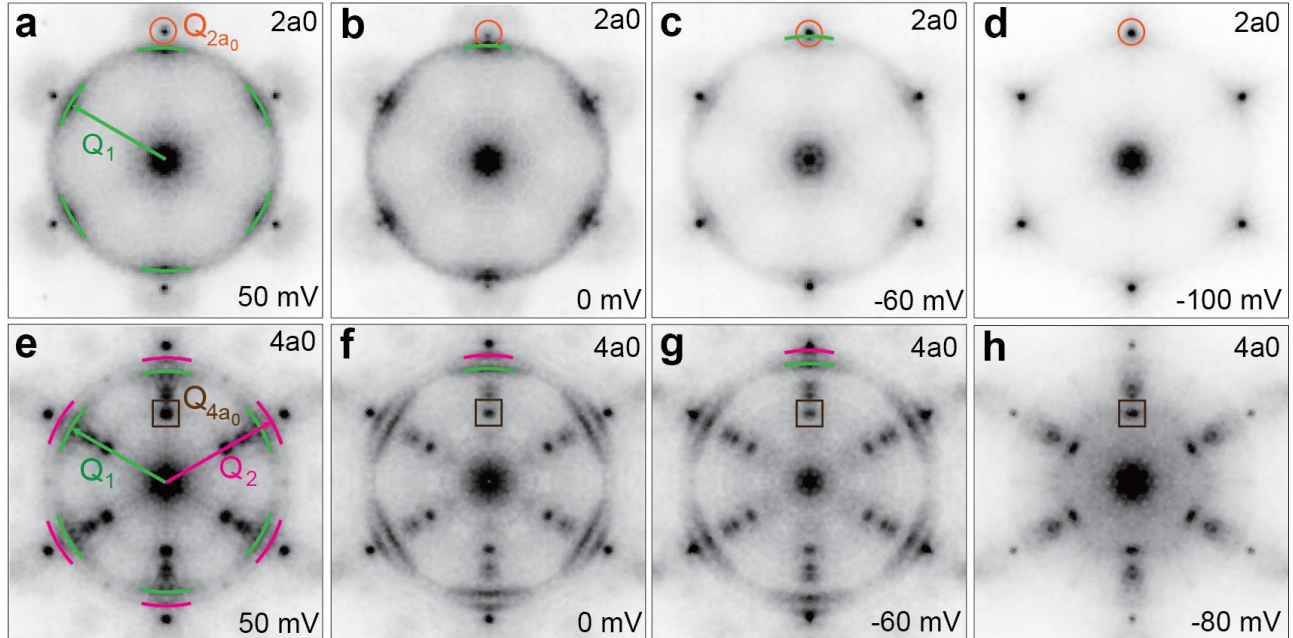


Figure S10. QPI evolution at low energies. FTs of dI/dV maps at different energies of regions hosting (a-d) CDW- $2a_0$ and (e-h) CDW- $4a_0$. All FTs have been 6-fold symmetrized. Prominent peaks are denoted as following: 1Q \mathbf{Q}_{4a_0} (brown square), 3Q \mathbf{Q}_{2a_0} (orange circles), \mathbf{Q}_1 (green lines) and \mathbf{Q}_2 (pink lines). CDW- $4a_0$ is a unidirectional order, so the six-fold symmetry of the \mathbf{Q}_{4a_0} peak in (e-h) is an artifact of the symmetrization process.

Section VI. Theoretical Model

The model employed in this work has previously been developed in Refs. ^{11,13,14} to simulate the charge order in $2H\text{-NbSe}_2$. Based on this model, the charge order stems from a strong electron-phonon coupling dependent on both the ingoing and outgoing electronic momenta in the scattering event, as well as the orbital composition of the electronic bands between which the scattering occurs. We use the explicit expression for the coupling in terms of purely electronic properties derived in Ref. ¹⁵.

The two bands at the Fermi level are composed primarily of the Niobium $d_{3z^2-r^2}$ orbitals ^{14,16}. We therefore work within a 2-band model, using the electronic dispersion obtained from a tight-binding fit to ARPES data in Ref. ¹⁷. The Random Phase Approximation (RPA) is used to calculate the softening of the phonon dispersion. The softened phonon frequency is given by:

$$\Omega_{RPA}^2(\mathbf{q}) = \Omega_0^2(\mathbf{q}) - \Omega_0(\mathbf{q})D_2(\mathbf{q})$$

where \mathbf{q} is the momentum-transfer wave vector, $\Omega_0(\mathbf{q})$ is the bare phonon dispersion and $D_2(\mathbf{q})$ is the full electronic susceptibility, including the matrix elements. In decreasing temperature, as soon as the phonon frequency first softens to zero, a CDW with the corresponding \mathbf{q} value results.

In order to find the geometry of the CDW in the ordered phase, we calculate the expression for the Landau free energy from the microscopic theory, keeping terms up to the fourth order ¹⁴. Then, we compare different orderings geometries to see which one minimizes the free energy. Note that $D_2(\mathbf{q})$ contributes to the quadratic term in the free energy expansion and is the same for both geometries. As the geometries break different symmetries their free energy expansions differ. That is, they have different coefficients in the free energy expansion (see Ref. ¹⁴ for further details).

Including Strain

To model the effect of strain on the electronic dispersion, we consider both volume-preserving deformations of the unit cell along a preferred in-plane axis (uniaxial strain), and isotropic changes in the unit cell volume (biaxial strain). We then assume that the hopping integrals depend linearly on the distance between atoms, with equal coefficient for all pairs of atoms considered. In both cases, the amount of strain is quantified by defining a dimensionless measure of strain σ in the hopping integral between nearest neighbor Nb atoms: $t = t_0(1 + \sigma)$. The corresponding expressions for hopping between further neighbors depend on σ , and an additional geometrical factor signifying how much the tunneling distance changed in comparison to that between nearest neighbors.

We separately include the effect of uniaxial in-plane strain on the phonons, by shifting the bare phonon energies differently in different lattice-equivalent directions. Along one Γ -M direction, we increase the phonon energy by d , and along the $2\pi/3$ -rotated directions we decrease the energy by $d/2$ (In accordance with the conserved unit cell volume).

On top of these considerations, we need to consider the fact that the Luttinger volume should be conserved in physical strain processes. To approximate the constant Luttinger volume in our model

across all strain levels considered, we adjust the chemical potential μ to keep the number of k -points contained within the Fermi surface approximately fixed.

Choice of Parameters

Within our model, we find that biaxial strain by itself has very little effect on the shape of $D_2(\mathbf{q})$, while uniaxial strain has a pronounced effect on the peak in the susceptibility curve (Fig. 4). In the main paper, we present the simplest model that captures the physics behind the formation of different CDWs, which relies exclusively on the uniaxial strain.

In choosing the parameters used in Fig. 4 of the main text, we require a good match to the electronic dispersion along the Γ -M direction as measured by QPI (Fig. 3 of the main text). We also require that the Luttinger volume stays approximately fixed when adding strain in the model. Note that we do not require the transition temperature to be maintained within any particular bounds. This is for two reasons. First, the transition temperatures are not known under strain. Second, it is known that transition temperatures predicted by RPA are generally too high, as the approximation fails to account for fluctuations in the phonon field, which are significant in NbSe₂ owing to its quasi-2D nature. The error can be corrected with higher-order diagrams, but this would not add new information to the present discussion^{11,18}.

Specifically, we consider two particular sets of parameter values in Figure 4. Using $\sigma = 0.1$ (measure of uniaxial strain level) and $\sigma_l = 0.0$ (measure of biaxial strain level) leads to a peak in the susceptibility curve between $0.25|\mathbf{Q}_{\text{Bragg}}|$ and $0.28|\mathbf{Q}_{\text{Bragg}}|$, and a 3Q order. Adding strain-induced anisotropy in the phonon dispersion on the same order as σ ($\sim 1.8\%$) is sufficient to break the symmetry of the predicted CDW order down to 1Q. With a chemical potential of $\mu = +60$ meV, the Luttinger volume stays within the bounds set by the precision of our measurements. In Figure S11, we show the electronic dispersion as deduced from our QPI measurements overlaid by the predictions of the RPA with these parameter values. In Figure S12, we show the Fermi surfaces predicted within our model calculations, together with the Fermi surfaces of the unstrained case (our model exactly matches ARPES measurements in the unstrained case by construction¹¹).

The values of $\sigma = -0.3$ and $\sigma_l = 0.0$ give a peak in the susceptibility centered at $\sim 0.4|\mathbf{Q}_{\text{Bragg}}|$. The order is found to be of 3Q type, as in the experimental observations, although small amounts of strain-induced phonon anisotropy will again favor 1Q order. Charge order developing so close to $0.5|\mathbf{Q}_{\text{Bragg}}|$ is expected to lock into the lattice and order at $0.5|\mathbf{Q}_{\text{Bragg}}|$ if the collective coupling of the CDW to the atomic lattice would be taken into account. With a chemical potential of $\mu = +20$ meV, the Luttinger volume is conserved to within 2%, although the Fermi surface appears to have qualitatively changed, owing to a saddle-point crossing the chemical potential. Using these values, the QPI dispersion is well matched, as shown in Figure S11.

Our model reveals that uniaxial strain is crucial for the formation of different CDW phases. An exact comparison between the changes in overlap integrals and the corresponding atomic strain levels is beyond the scope of the current paper, as it requires simultaneous consideration of the electronic kinetic and potential energies, as well as the phonon spectrum and electron-phonon coupling. It was shown in Ref. ¹⁹, however, that d -orbital overlap integrals generically scale with the inverse fifth

power of inter-atomic distance. Based on this, we can roughly estimate $\sigma = (t-t_0)/t_0 \sim -5 (r-r_0)/r_0$. That is, the fitted changes in overlap integral should correspond roughly to five times the relative strain defined in the experimental analysis. Using this simple approximation, we proceed to discuss in detail the extent to which our model matches experimental observations:

- Based on the theoretical model, CDW- $4a_0$ phase accompanies a uniaxial strain simulated by $\sigma = 0.1$ (stretching along Γ -M by $\sim 2\%$ and the compression along Γ -K by $\sim 2\%$). From the experimental data in Figure S7(b), the dominant strain eigenvector averaged over the CDW- $4a_0$ area has $\sim 2.3\%$ magnitude and the direction of stretching points ~ 23 degrees with respect to the nearest Γ -M direction.
- Based on the theoretical model, CDW- $2a_0$ phase accompanies a uniaxial strain simulated by $\sigma = -0.3$ (compression along Γ -M by $\sim 6\%$ and stretching along Γ -K by $\sim 6\%$). From the experimental data in Figure S7(a), the dominant strain eigenvector averaged over the CDW- $2a_0$ area has $\sim 2.5\%$ magnitude and the direction of stretching points ~ 12 degrees with respect to the nearest Γ -K direction.

As discussed above, we attribute the difference in the strain magnitudes to the simplicity of the formula used to relate the orbital overlap in theory and experimental strain, which does not take into account several important physical factors. We also note again that atomic-scale strain observed in experiments assumes no strain in the CDW- $3a_0$ area. However, even a small residual strain the CDW- $3a_0$ area can have a significant effect in the resulting direction of the measured strain with respect to the high symmetry directions, and as such could explain the difference in the observed angle of strain components between theory and experiment above.

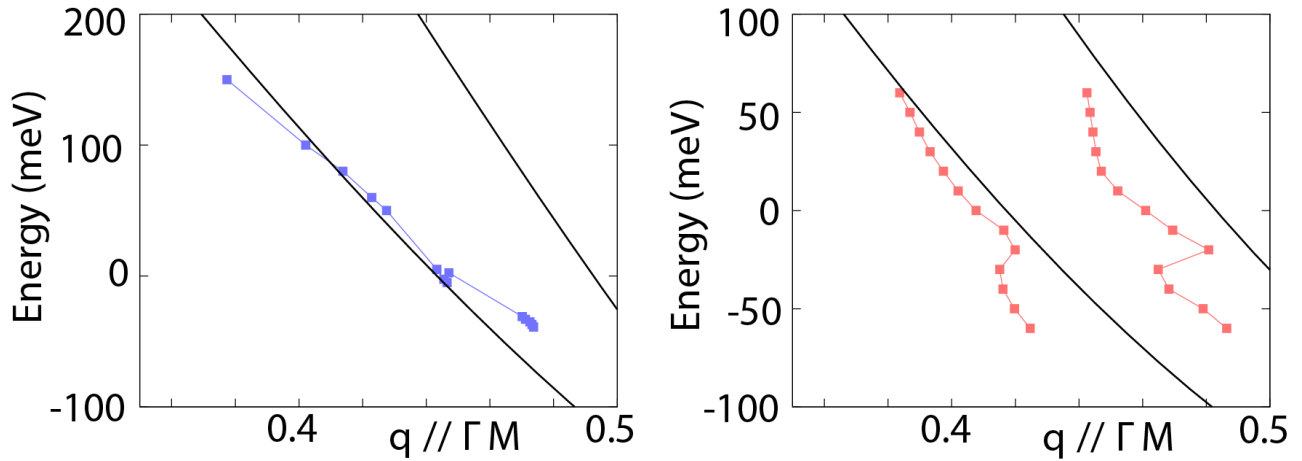


Figure S11. Comparison to QPI data. *Left:* QPI-measured electronic dispersion along the Γ -M direction (blue), as found in regions of the sample with CDW- $2a_0$ order, and the dispersion predicted by the model with strain leading to a CDW wavevector of $\sim 0.4|\mathbf{Q}_{\text{Bragg}}|$ (black line), which would be expected to lock into a commensurate CDW- $2a_0$ structure. *Right:* QPI-measured dispersion along Γ -M in regions of CDW- $4a_0$ order (red lines), and the dispersion predicted by the model with strain leading to wavevector $0.25|\mathbf{Q}_{\text{Bragg}}|$ (black lines).

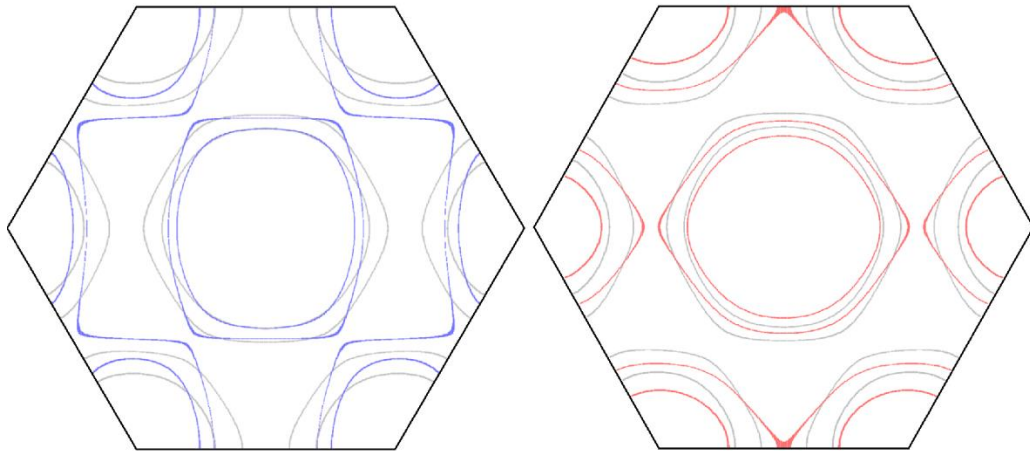


Figure S12. Fermi surfaces under strain. The result with parameters set to give a CDW with the wave vector of $\sim 0.4|\mathbf{Q}_{\text{Bragg}}|$ (left, blue), and the wave vector of $\sim 0.25|\mathbf{Q}_{\text{Bragg}}|$ (right, red). In both panels, the grey lines show the unstrained Fermi surface from the model, which matches ARPES measurements¹⁷ by construction.

Section VII. Dual geometry of CDW- $2a_0$

At low bias (Figure S13(a,b)), although dark regions exhibit a triangular CDW- $2a_0$ running uniformly along all lattice directions, bright regions are showing signs of selecting a preferred direction. This becomes apparent in the STM topograph at higher bias in Figure S13(c), where each bright region exhibits a unidirectional CDW- $2a_0$ order. Since this stripe CDW order exhibits different directions in different regions of the sample within the same field-of-view (denoted by arrows in Figure S13(b,c)), such behavior cannot be attributed to STM tip directionality. Our theoretical calculations in Fig. 4 of the main text indeed predict that both unidirectional and triangular CDW- $2a_0$ can be stabilized, which is experimentally confirmed here.

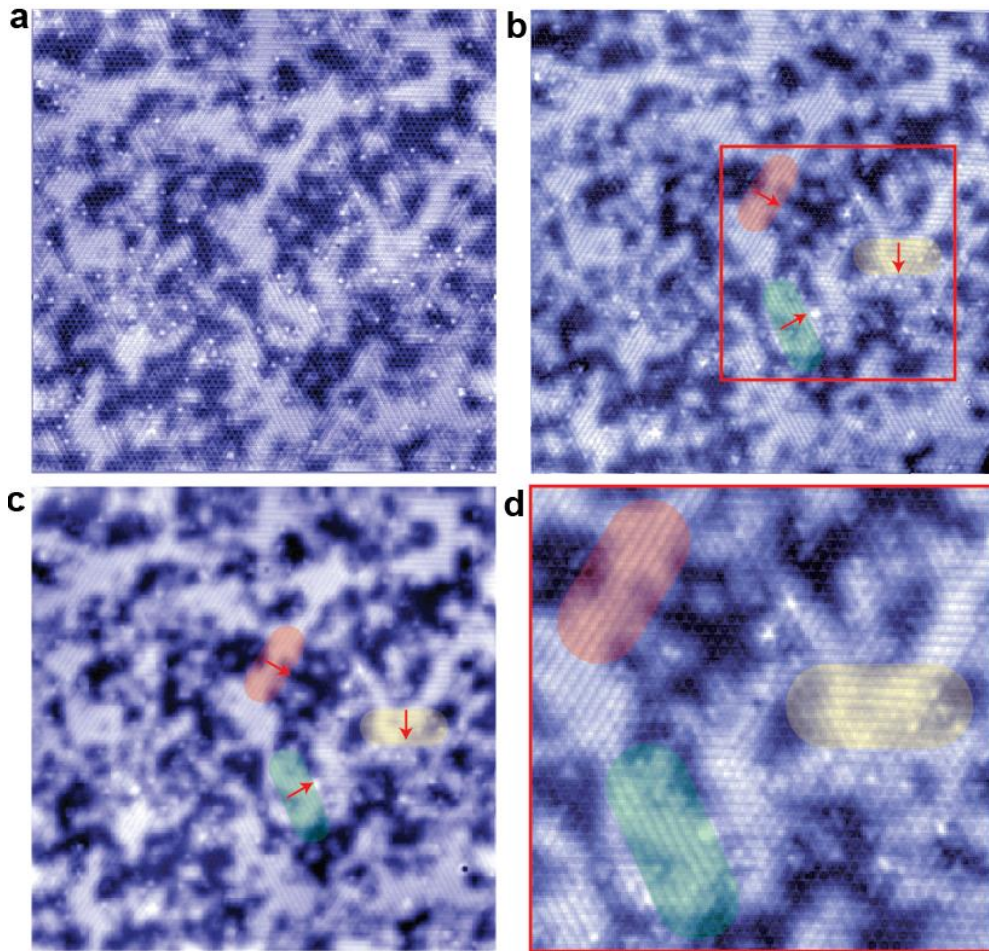


Figure S13. Different geometries of CDW- $2a_0$ observed at different energies. STM topographs of the same region of the sample hosting CDW- $2a_0$, acquired at (a) -200mV/500pA, (b) 150mV/400pA and (c) 250mV/600pA. (d) Zoom-in on the red square in (b). Red arrows in all panels denote the direction of the 1Q CDW wavevector.

Section VIII. Large domain size of observed CDWs

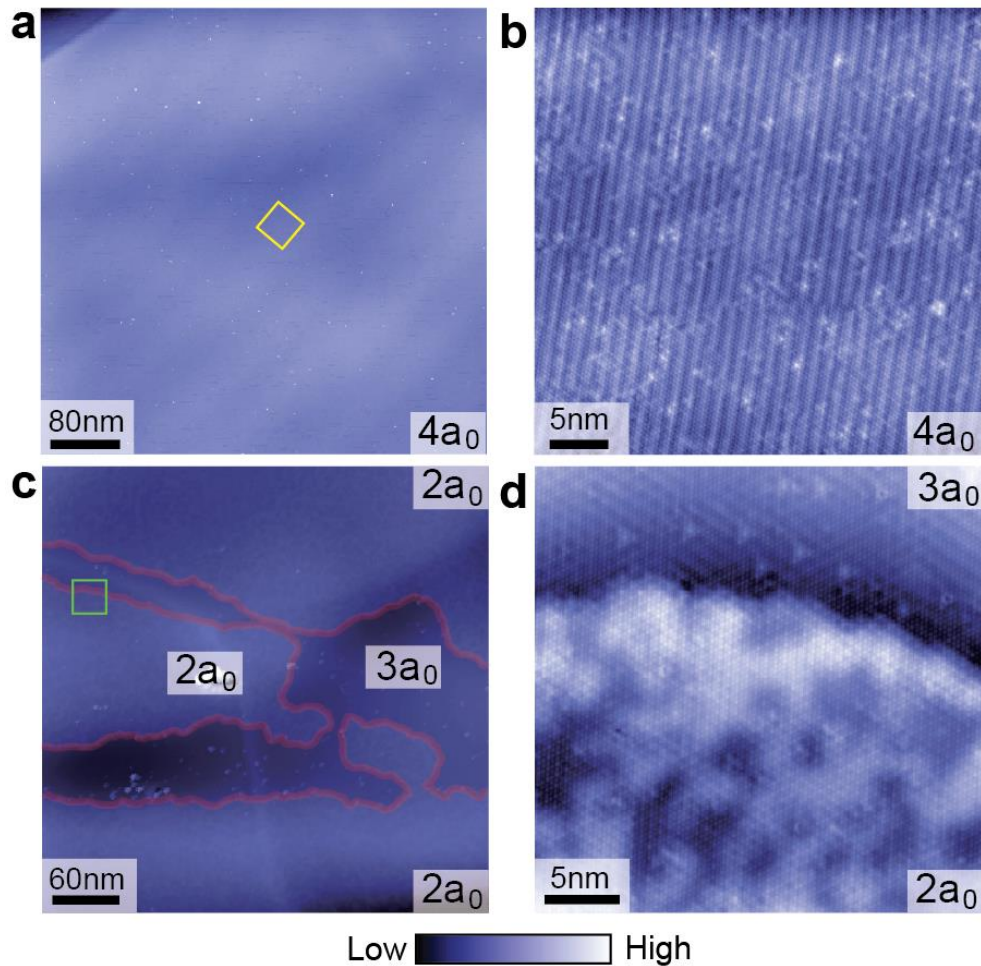


Figure S14. Large-scale STM topographs of CDW-4a₀ and CDW-2a₀ area. (a) STM topograph of a 510 nm square region of the sample hosting predominantly CDW-4a₀. (b) Close-up STM topograph corresponding to the yellow square in (a). (c) STM topograph of a 400 nm square region hosting CDW-2a₀ over the majority of the area. The superimposed red lines separate the regions hosting CDW-2a₀ and CDW-3a₀. (d) Close-up STM topograph of the area inside the green square in (c).

Section IX. Sample growth, characterization and strain setup

Single crystal of NbSe₂ was grown in two steps, using chemical vapor transport method with I₂ as a transport agent. Silica ampoule (20-30 cm long, 1.8 cm inner diameter and 2.0 mm outer diameter) was used for the synthesis and growth. In the first step, for direct solid state reaction, stoichiometric amount of Nb:Se (5N purity of precursors) in 1:2 ratio was taken into a quartz ampoule and evacuated followed by sealing under vacuum. Then, the ampoule containing the mixture was placed in a furnace with the temperature of ~600 °C for one week and then cooled down to room temperature. The resultant product of NbSe₂ was obtained with a single phase. In the second step, a muffle furnace with two-zones was fabricated for this purpose. The synthesized polycrystalline powder of NbSe₂ with I₂ was taken in a quartz ampoule and placed in furnace maintaining the temperature 800-825 °C. After the period of 15 days, single crystals of NbSe₂ were obtained. Subsequent magnetization measurements demonstrate the onset of superconductivity at $T_c \sim 7$ K (Figure S15).

We used standard silver epoxy (EPO-TEK H20E) to attach a piece of NbSe₂ single crystal to a commercial piece of silica (dimensions 4 mm x 4 mm x 0.5 mm). The process was done under the optical microscope and the epoxy was applied by hand. The epoxy was typically cured at ~150 °C. One side of silica is then rigidly attached to our STM sample holder by a clamp. The bias contact to the sample is ensured by making a conducting path from the bottom of NbSe₂ to the metallic part of the sample holder by a thin line of silver epoxy. Typical size of the single crystals used before cleaving was ~ 2 mm by 2 mm, with ~0.1 mm thickness. The thickness was determined by: (1) imaging the side surface by optical methods, and (2) measuring the lateral size and weight to determine the thickness. Both methods gave comparable results. Based on our experience in

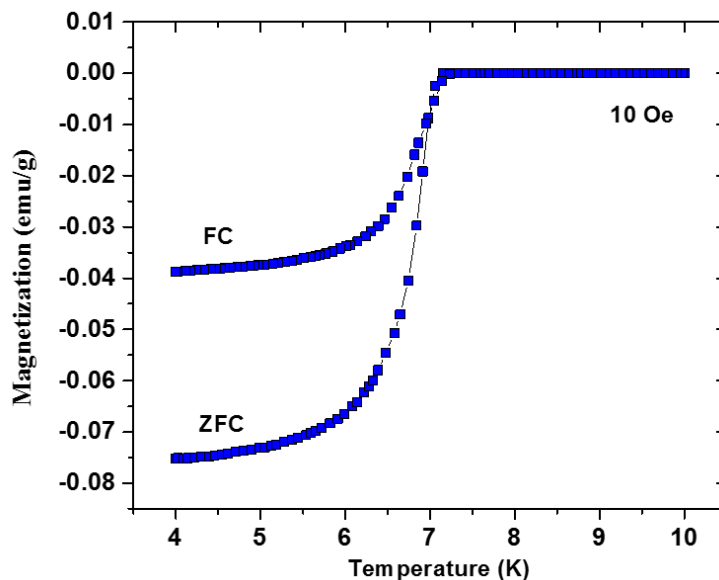


Figure S15. Ex-situ magnetization measurements. Zero-field-cooled (ZFC) and field-cooled (FC) magnetization measurements of NbSe₂ acquired in 10 Oe magnetic field, showing the onset of diamagnetic response due to Meissner effect at $T_c \sim 7$ K.

cleaving various van der Waals materials, post-cleaved thickness is reduced anywhere from ~ 0 to an order of magnitude, so we can provide a rough estimate of the thickness of the samples studied by STM to be from 10-100 micrometers. We note that our samples are highly unlikely to be in the thin film limit where we need to take into account finite z-dimension effects in the interpretation of our data.

We studied 4 different NbSe₂ crystals glued on silica (5 different surfaces as one sample was re-cleaved for the second approach). For each of these 5, we approached the tip on several microscopically different points on the sample, which are typically tens of micrometers away from one another, and searched for different types of CDWs. We observed: all three CDWs on 2 surfaces, just CDW-2a₀ and CDW-4a₀ on two other surfaces, and just CDW-3a₀ on one surface.

References

1. Lawler, M. J. *et al.* Intra-unit-cell electronic nematicity of the high-T_c copper-oxide pseudogap states. *Nature* **466**, 347–351 (2010).
2. Zeljkovic, I. *et al.* Scanning tunnelling microscopy imaging of symmetry-breaking structural distortion in the bismuth-based cuprate superconductors. *Nat. Mater.* **11**, 585–9 (2012).
3. Zeljkovic, I. *et al.* Mapping the unconventional orbital texture in topological crystalline insulators. *Nat. Phys.* **10**, 572–577 (2014).
4. Wang, Z. *et al.* Quasiparticle interference and strong electron-mode coupling in the quasi-one-dimensional bands of Sr₂RuO₄. *Nat. Phys.* **13**, 799–805 (2017).
5. Landau, L. D. & Lifshitz, E. M. *Theory of Elasticity.* (1960).
6. Soumyanarayanan, A. *et al.* Quantum phase transition from triangular to stripe charge order in NbSe₂. *Proc. Natl. Acad. Sci.* **110**, 1623–1627 (2013).
7. Kadijk, F. & Jellinek, F. On the polymorphism of niobium diselenide. *J. Less Common Met.* **23**, 437–441 (1971).
8. Nakata, Y. *et al.* Monolayer 1T-NbSe₂ as a Mott insulator. *NPG Asia Mater.* **8**, e321–e321 (2016).
9. Arguello, C. J. *et al.* Quasiparticle interference, quasiparticle interactions, and the origin of the charge density wave in 2H-NbSe₂. *Phys. Rev. Lett.* **114**, 37001 (2015).
10. Borisenko, S. V. *et al.* Two energy gaps and fermi-surface ‘arcs’ in NbSe₂. *Phys. Rev. Lett.* **102**, 166402 (2009).
11. Flicker, F. & van Wezel, J. Charge order from orbital-dependent coupling evidenced by NbSe₂. *Nat. Commun.* **6**, 7034 (2015).
12. Zhao, J. *et al.* Orbital selectivity causing anisotropy and particle-hole asymmetry in the charge density wave gap of 2H-TaS₂. *Phys. Rev. B* **96**, 125103 (2017).
13. Flicker, F. & van Wezel, J. Charge ordering geometries in uniaxially strained NbSe₂. *Phys. Rev. B* **92**, 201103 (2015).
14. Flicker, F. & van Wezel, J. Charge order in NbSe₂. *Phys. Rev. B* **94**, 235135 (2016).
15. Varma, C. M. & Weber, W. Phonon dispersion in transition metals. *Phys. Rev. B* **19**, 6142–6154 (1979).
16. Doran, N. J., Titterington, D. J., Ricco, B. & Wexler, G. A tight binding fit to the bandstructure of 2H-NbSe₂ and NbS₂. *J. Phys. C Solid State Phys.* **11**, 685–698 (1978).
17. Rossnagel, K. On the origin of charge-density waves in select layered transition-metal dichalcogenides. *J. Phys.*

Condens. Matter **23**, 213001 (2011).

18. Varma, C. M. & Simons, A. L. Strong-Coupling Theory of Charge-Density-Wave Transitions. *Phys. Rev. Lett.* **51**, 138–141 (1983).
19. Wills, J. M. & Harrison, W. A. Interionic interactions in transition metals. *Phys. Rev. B* **28**, 4363–4373 (1983).